Phase-Field Simulation of Solidification Behavior of AlSi10Mg Alloys Manufactured Through Direct Metal Laser Sintering

Hossein Azizi, Alireza Ebrahimi, Nana Ofori-Opoku, Michael Greenwood, Nikolas Provatas and Mohsen Mohammadi

Abstract In this work, we numerically investigate the effect of building direction on the solidification behaviour and microstructure evolution of direct metal laser sintered (DMLS) AlSi10Mg. The building direction, as previously proved in experimental studies, can influence the solidification behavior and promote morphological transitions in cellular dendritic microstructures such as columnar-to-equiaxed transition (CET). We develop a thermal model to systemically address the impact of laser processing conditions and building direction on time-dependent solidification parameters including pulling velocity, thermal gradients, and cooling rates of the molten pool during DMLS of AlSi10Mg alloy. We then study the microstructure evolution of DLMS-AlSi10Mg for horizontal and vertical building directions. The present model includes heterogenous nucleation on inoculant particles that triggers the CET, and its results are consistent with the predictions of a previously developed

H. Azizi (✉) · A. Ebrahimi · M. Mohammadi
Marine Additive Manufacturing Centre of Excellence (MAMCE),
University of New Brunswick, Fredericton, NB E3B 5A3, Canada
e-mail: hazizi@unb.ca

A. Ebrahimi
e-mail: Alireza.Ebrahimi@unb.ca

M. Mohammadi
e-mail: Mohsen.Mohammadi@unb.ca

N. Ofori-Opoku
Computational Techniques Branch, Canadian Nuclear Laboratories,
Chalk River, ON K0J 1J0, Canada
e-mail: nana.ofori-opoku@cnl.ca

M. Greenwood
CanmetMATERIALS, Natural Resources Canada, 183 Longwood Road south,
Hamilton, ON L8P 0A5, Canada
e-mail: michael.greenwood@canada.ca

N. Provatas
Physics department, and Centre for the Physics of Materials, McGill University, 3600 University street,
Montreal, QC H3A-2T8, Canada
e-mail: nick.provatas@mcgill.ca

model. In addition, findings are compared with experimental observations to ensure the accuracy of obtained numerical results.

Keywords Columnar-to-equiaxed transition · AlSi10Mg · Phase-field simulation · Direct metal laser sintering (DMLS)

Introduction

Among the available additive manufacturing (AM) processes, direct metal laser sintering (DMLS) has been accepted as a new paradigm for the design and production of high performance complex components. This is due to its unique features, such as fast solidification rate, short manufacturing times, and controlled melting and solidification processes [8]. This process is widely known to be a well-suited technique for processing aluminum alloy powder, in particular AlSi10Mg [9]. DMLS-AlSi10Mg has attracted much attention recently due to its mechanical and structural properties suited to applications in aerospace, automotive, and marine industries [6].

Significant effort has been made to study the evolution of grain structure during AM processes [13]. It is shown by these studies that despite the complexities involved in AM processes, the evolution of grain structure for a given set of parameters can be determined by thermal gradient G, solidification rate R, and undercooling ΔT [7]. Two widely observed solidification microstructures in AM processes are columnar and equiaxed structures [13]. Under certain conditions when sufficiently large number of equiaxed dendrites nucleate in the constitutionally undercooled liquid adjacent to the solidification front, columnar grains are terminated with the formation of equiaxed grains and a columnar-to-equiaxed transition (CET) takes place [5]. In recent years, numerous experimental and computational studies have been carried out to investigate the CET occurring in DMLS processes. For instance, Hadadzadeh et al. [6] conducted an experimental study to inspect the microstructure of AlSi10Mg alloy processed by the DMLS technique using different building directions. Their observations clearly confirmed the formation of CET structures. The authors also showed that changes to the building direction can affect both columnar-to-equiaxed ratio and the texture of DMLS-AlSi10Mg alloy. These effects are clearly illustrated in EBSD images for two horizontal and vertical samples (Fig. 1).

The main purpose of this work is to understand the mechanism of crystal orientation selection for given thermal conditions of the DMLS process. We develop a thermal model to extract laser thermal parameters and then simulate the microstruture evolution by employing a phase-field model for the resultant thermal conditions. A new efficient numerical approach to capture the heterogeneous nucleation that triggers CET is introduced. These are used to continue our investigation to explore the texture of DMLS-AlSi10Mg alloy for different processing parameters and build directions. The results of this study will be reported in an upcoming publication.

In this work, we make the following approximations of the alloy to simplify the initial test simulations:
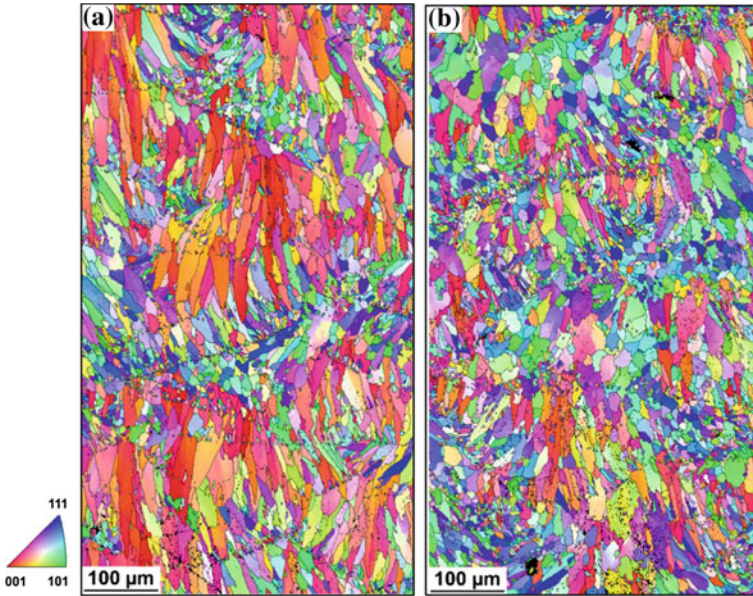
Fig. 1 EBSD IPF-Z images of **a** vertical and **b** horizontal samples superimposed with grain boundaries. The figure is adopted from [6]

1. We focus on the solidification of a binary AlSi alloy. The concentration of magnesium in AlSi10Mg is low. Evaporation during the DMLS process further reduces this concentration. Its effect on the microstructure evolution appears to be minimal, and therefore, we omit it from the simulations.
2. We choose to study the solidification of binary AlSi alloy in the dilute limit. The solute (Si) concentration is set to a very small value (0.5 wt.%) which is more consistent with the dilute alloy limit assumption.

Free Growth Phase-Field Model

we employ an adaptation of the model of Ofori-Opoku and Provatas [10] formulated from grand potential functional [11], which allows us to model the evolution of the chemical potential field alongside the order parameters representing grains. The details of the model are found in [4, 12]. We performed our numerical phase-field simulations of solidifying domains within a 2-D system using the same numerical techniques discussed previously in [1]. In this model, the order parameter vector is defined as $\vec{\phi}(\vec{r}) = \left(\phi_1(\vec{r}), \phi_2(\vec{r}), \ldots, \phi_N(\vec{r})\right)$, whose components are bounded by 0 and 1, representing the bulk of liquid and solid phases, respectively. Each order parameter ϕ_i represents one of N distinct solid grain orientations or crystal structures

at a particular point in a volume. Through their interactions, they always satisfy $\phi_1 + \phi_2 + \cdots + \phi_N \leq 1$ [4]. The solid–liquid interface is represented as a region with finite (but nonzero) thickness W_i in which the order parameter ϕ_i varies, continuously, between its two bulk values.

The grand potential functional for a multi-phase dilute binary system can be written in the following form [11]:

$$\Omega[\vec{\phi}, \mu] = \int dv \left\{ \omega_{\text{int}}(\vec{\phi}, \vec{\nabla}\phi) + \sum_{\alpha=1}^{N} g_\alpha(\vec{\phi})\, \omega^\alpha(\mu) + \left[1 - \sum_{\alpha=1}^{N} g_\alpha(\vec{\phi}) \right] \omega^l(\mu) \right\},$$
(1)

where ω and μ are the grand potential density and chemical potential, respectively, l is the liquid phase, and index α runs over solid phases or orientations. The first term in Eq. (1) accounts for the interaction energy between order parameters, while the remaining terms are the grand potential densities of the bulk solid and liquid phases. The functions $g_\alpha(\vec{\phi})$ interpolate the local grand potential density between phases via the order parameter components ϕ_α.

The dynamics of the solidification in the grand potential formalism is described by the evolution of each order parameter ϕ_α and chemical potential of the solute species μ:

$$\frac{\partial \phi_\alpha}{\partial t} = -M_{\phi_\alpha} \frac{\delta \Omega}{\delta \phi_\alpha} + \xi_\phi,$$
(2)

$$\frac{\partial \mu}{\partial t} = \frac{1}{\chi} \left[\nabla \cdot \left(M(\vec{\phi}, c)\, \nabla \mu \right) - \sum_\alpha g_\alpha'(\vec{\phi}) \left(c^\alpha(\mu) - c^l(\mu) \right) \frac{\partial \phi_\alpha}{\partial t} \right] - \nabla \cdot \vec{\zeta}, \quad (3)$$

where M_{ϕ_α} defines a suitable time scale of ϕ_α, $M(\vec{\phi}, c)$ is Osanger-type mobility coefficient for mass transport, and χ is the susceptibility parameter that is defined as $\partial c / \partial \mu$. The stochastic fields ξ and $\vec{\zeta}$ in Eqs. (2) and (3) account for thermal fluctuations in order parameters and noise flux governing fluctuations in solute concentration, respectively [12].

Nucleation

In this study, we solely consider heterogeneous nucleation on partially melted powders (inoculants) as the dominant mechanism of CET [2]. In order to examine the spontaneous nuclei formation in an undercooled liquid, we take the same approach as discussed previously in [1]. In this method, the energy barrier of solid–liquid nucleation within a volume ΔV (surface ΔA in 2-D) of an inoculant, is set to its corresponding value for heterogenous nucleation for a given contact angle θ. The free energy barrier for heterogenous nucleation for a given set of conditions (solute

concentration and temperature) is calculated according to classical nucleation theory and can be written as,

$$\Delta F^* = \frac{16\,\pi}{3} \frac{h(\theta)\,\gamma^3}{\Delta f_v^{\,2}},$$ (4)

where γ is the interfacial energy $(\mathrm{J/m^2})$, h is a heterogenous pre-factor that depends on the contact angle θ, and Δf_v is the bulk free energy change per unit volume $(\mathrm{J/m^3})$. The contact angle θ depends on the interfacial energy between the liquid and the surface of an inoculant particle.

Heterogeneous nucleation is controlled by redefining the dimensionless lambda parameter λ that enters the quantitative phase-field model [3], as a quenched in field whose values depend on local solute concentration in undercooled liquid and contact angle, and can be written in the following form,

$$\lambda_{\text{het}} = \frac{1}{2} \frac{I\,W\,\Delta f_v}{\gamma\,\sqrt{h(\theta)}}.$$ (5)

Fluctuations that lead to nucleated order parameters are affected in a separate system, that interacts with the grains in the main simulation domain, but not vice versa. Once an order parameter is triggered, it is added to the main simulation domain. Within the main simulation of domain of free-growing crystals, the value of lambda is set to a constant in the entire domain.

Thermal Modelling

The thermal profile of DLMS-AlSi10Mg is calculated for two horizontal and vertical printing strategies using the finite element method (FEM). The sample sizes for horizontal and vertical samples in (x, y, z) coordinates are set to $10\,\mathrm{mm} \times 10\,\mathrm{mm} \times 1\,\mathrm{cm}$ and $2.5\,\mathrm{mm} \times 2.5\,\mathrm{mm} \times 1\,\mathrm{cm}$, respectively. In both cases, the whole body is assumed to be fabricated (i.e. in solid phase) while the focus of modeling is on the last powder layer with a thickness of $z = 30\,\mu\mathrm{m}$. The laser processing parameters that we used in our model can be found in Table 1. In this model, heat generation by laser is represented by a Gaussian heat source while heat dissipation mechanism is modeled as heat convection and radiation on the top surface (i.e. $z = 0$), and conduction through the base metal. To accurately simulate the melting and subsequent solidification processes, the phase change from powder to liquid and liquid to solid phases are taken into account.

Table 1 Processing parameters of DMLS-AlSi10Mg

Scan speed (ms^{-1})	1.3
Laser power (W)	370
Laser spot size (mm)	0.05
Layer thickness (mm)	0.03
Preheat temperature (K)	473.15
Density (kgm^{-3})	2650
Latent heat (Jkg^{-1})	389,187
Thermal diffusivity (m^{2}s^{-1})	4×10^{-5}
Convective heat transfer (Wm^{-2} K^{-1})	80
Emissivity	0.19

Results and Discussion

In this section, we briefly discuss the solidification process in a vertically fabricated sample to demonstrate the effect of laser processing conditions in the DMLS-AlSi binary alloy on the microstructure evolution. A more complete investigation of different build directions is related to a forthcoming publication.

Phase-field simulations were conducted for solidification of a vertically printed part in a 2-D computational domain with a size of 240 μm × 45 mm, along the direction of laser propagation x, and depth of the melt pool z. All relevant parameters used in our simulation are summarized in Table 2. We initiate the simulation by setting up an initial solid–liquid interface and solute composition profile based on the imposed thermal profile of the melt pool. The interface is then evolved using the corresponding transient laser thermal profile.

The results of these simulations are depicted in Fig. 2. Figure 2 shows the solute (Si) concentration map for two instances in the evolution of solidification (Fig. 2a: after initial nucleation events and Fig. 2b: after complete solidification). At the early stages of the simulation, several nuclei have emerged with random orientations which continue to grow, driven by the local thermal gradient (heat extraction).

The formation of these nuclei can be attributed to the high thermal gradient in the vicinity of the top surface. These grains collectively form a second propagating solid–liquid interface moving downward. Both downward and upward solidification fronts merge at the trailing end of the melt pool forming a fully solidified part. The formation of these two fronts is proposed to be by the effective heat extraction at the top surface and due to the heat conduction through the bulk material at the bottom.

Among all the grains with different orientations that nucleated initially, only those that are more aligned with the temperature gradient tend to grow faster and thus outgrow slower misaligned dendrites.

Table 2 Physical properties of AlSi binary alloy, phase-field, and nucleation parameters used in the simulations

Physical properties	
Chemical composition (wt.%)	Al: 99.5, Si: 0.5
Melting point of Al (K)	932.85
Liquid slope (°C wt.%$^{-1}$)	6.5
Partition coefficient, k_e	0.13
Solute diffusivity (liquid; m^{2}s^{-1})	3×10^{-9}
Solute diffusivity (solid; m^{2}s^{-1})	1×10^{-12}
Gibbs–Thomson coefficient (K m)	9×10^{-8}
Phase-field parameters	
Effective interface width, W_o (m)	2.5×10^{-8}
Relaxation time, τ_o (s)	5.7×10^{-7}
Minimum grid spacing, dx	$0.8\,W_o$
Anti-trapping coefficient	0.35355
Nucleation parameters	
Inoculant number density, N_p (m^{-3})	1.2×10^{14}
Heterogenous pre-factor, h	3×10^{-4}
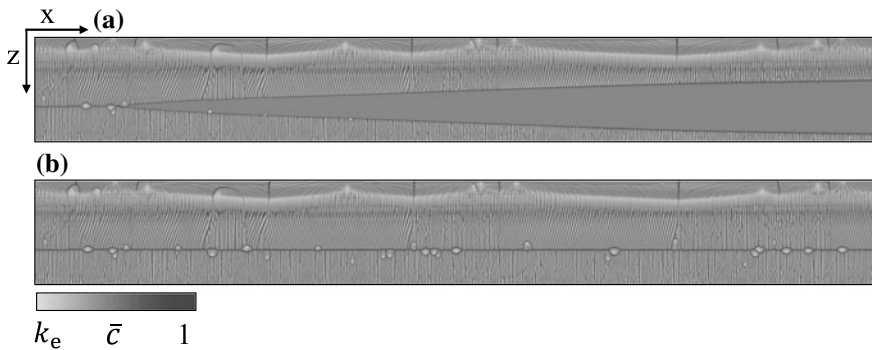
Fig. 2 Concentration map of solute (Si) for a single powder layer with vertical build direction: **a** after initial nucleation events and **b** after complete solidification. The direction of laser propagation is to the right (depicted by x arrow). The bottom layer has grown from a base metal layer initiated in the simulation. The top layer ($z = 0$) comprises several heterogeneous nucleation events on the top melted liquid layer. The colour bar shows the dimensionless solute concentration scale

The final stage of the simulation is displayed in Fig. 2b. The nucleation events observed between the two propagating fronts are the result of the constitutional undercooled liquid entrapped between them. We observe that the nucleation density is much less than the inoculant density. We propose two possible explanations for this. First, large thermal gradients G along with relatively fast solidification rates R give rise to very high cooling rates $CR = G \times R$ which effectively reduce constitutional undercooling and create a suppression of further nucleation events. Second, as the

solidification front progresses, it rejects more solute into liquid which increases the solute concentration in the vicinity of solid–liquid interface. This results in the liquid in between the two approaching interfaces to become highly saturated (i.e. liquid's concentration is very close to its equilibrium value at a given temperature), and therefore, further nucleation of equiaxed grains in these regions becomes very difficult.

Conclusion

In this work, we conduct a numerical study to investigate grain growth and columnar-to-equiaxed transition (CET) in dilute binary AlSi alloy, under thermal conditions of direct metal laser sintering process. A new 2-D phase-field model is utilized where we have incorporated a nucleation mechanism during free growth to simulate the coupled microstructure evolution process. Our simulation results for a vertically sintered single powder layer indicate that final grain structures are mainly comprised of columnar dendrites. We hypothesize that effect stems primarily from the high cooling rates involved in the process. However, to confirm this, further investigation of the effect of build direction (i.e. vertical and horizontal) on the time-dependent solidification parameters and the emerging microstructure is required. A thorough study of solidification behaviour for laser processing parameters will be conducted in an upcoming publication.

References

1. Azizi H, Provatas N, Mohammadi M (2019) Phase-field simulation of microstructure evolution in direct metal laser sintered AlSi10Mg. In: TMS 2019 148th annual meeting & exhibition supplemental proceedings, pp 311–318
2. Castro M (2003) Phase-field approach to heterogeneous nucleation. Phys Rev B 67(3):035412
3. Echebarria B, Folch R, Karma A, Plapp M (2004) Quantitative phase-field model of alloy solidification. Phys Rev E 70(6):061604
4. Greenwood M, Shampur K, Ofori-Opoku N, Pinomaa T, Wang L, Gurevich S, Provatas N (2018) Quantitative 3d phase field modelling of solidification using next-generation adaptive mesh refinement. Comput Mater Sci 142:153–171
5. Gäumann M, Bezencon C, Canalis P, Kurz W (2001) Single-crystal laser deposition of super-alloys: processing-microstructure maps. Acta Materialia 49(6):1051–1062

6. Hadadzadeh A, Amirkhiz BS, Li J, Mohammadi M (2018) Columnar to equiaxed transition during direct metal laser sintering of alsi10mg alloy: effect of building direction. Add Manuf 23:121–131
7. Kurz W, Giovanola B, Trivedi R (1986) Theory of microstructural development during rapid solidification. J Acta Metal 34:823–830
8. Li X, Ji G, Chen Z, Addad A, Wu Y, Wang H, Vleugels J, Van Humbeeck J, Kruth JP (2017) Selective laser melting of nano-tib2 decorated AlSi10mg alloy with high fracture strength and ductility. Acta Mater 129:183–193
9. Olakanmi EOT, Cochrane R, Dalgarno K (2015) A review on selective laser sintering/melting (sls/slm) of aluminium alloy powders: processing, microstructure, and properties. Prog Mater Sci 74:401–477
10. Ofori-Opoku N, Provatas N (2010) A quantitative multi-phase field model of polycrystalline alloy solidification. Acta Mater 58(6):2155–2164
11. Plapp M (2011) Unified derivation of phase-field models for alloy solidification from a grand-potential functional. Phys Rev E 84(3):031601
12. Shampur K (2017) A grand potential based multi-phase field model for alloy solidification. Master's thesis, Mcgill University
13. Wang T, Zhu Y, Zhang S, Tang H, Wang H (2015) Grain morphology evolution behavior of titanium alloy components during laser melting deposition additive manufacturing. J Alloys Comp 632:505–513